

A multi-channel framework for joint reconstruction of multi-contrast parallel MRI

Erfan Ebrahim Esfahani

Abstract—Compressed sensing, multi-contrast and parallel imaging are all techniques that exploit certain types of redundancies to speed up image acquisition process and image quality in MRI. Although each individual category has been well developed, the combination of the three has not received significant attention, much less the potential benefit of isotropy within such a setting. In this paper, a novel isotropic multi-channel image regularizer is introduced, and its full potential is unleashed by integrating it into compressed multi-contrast multi-coil MRI.

Index Terms—Magnetic Resonance Imaging (MRI), Multi-contrast Imaging, Parallel Imaging, Compressed Sensing, Variational Image Processing, Iterative Image Reconstruction.

I. INTRODUCTION, BACKGROUND AND RELATED WORK

MAGNETIC resonance imaging is perhaps the most popular medical imaging modality, basically because of its non-invasiveness, lack of hazardous radiation and excellent visualization. However, the slow data acquisition procedure inherent in this machine has forced researchers to resort to various redundancies abundant in MRI data to speed up the process. Compressed sensing (CS), multi-contrast (MC) and parallel imaging (PI) are various approaches that exploit specific types of such redundancies. In CS, sparse representations of the underlying image in certain transform domains are used to reduce the acquired data [1]. Since certain features (or lesions) are only observable in one contrast (and not all contrasts), MC imaging of the same anatomy helps to detect such a feature, where different contrasts make up for each other's deficits. However, except for the contrast-specific features, many other details such as edges preserve the same layout across contrasts, which might be a useful redundancy. In PI [2], multiple receive coils are placed around the object and each coil best detects the signals emitted from a specific region, depending on its sensitivity map. All regions could be imaged simultaneously, speeding up the whole sequence.

Single-coil single-contrast CS is the most extensively studied of the three techniques, some showpiece examples of which are [19], [4], [18], [12], [17], [15], [9]. The methods use various priors such as sparsity in finite-differences transform-domains etc to improve results. Similar ideas have been used in MC imaging where sparsity is imposed on multiple contrasts rather than just one, which yields additional information than a single contrast. In [5] a multi-channel version of the classical total variation was introduced for color image processing. In [6] CTV and joint sparsity are used to share cross-contrast details while conventional TV and single-channel sparsity

are used to preserve contrast-specific details. In [7] a multi-channel TV based on nuclear norm coupling of image gradient fields is used for multi-channel spectral CT. In [8] new versions of total variation (TV) are introduced for MC-MRI where local and directional manipulations are incorporated into TV formulation. However, these methods are restricted to 2 contrasts only, and PI is also not considered. With a slightly different taste, in [20] a multi-channel version of total generalized variation (TGV) [4] is presented for MR-PET reconstruction, based on nuclear norm minimization. This method considers PI but is still restricted to 2 channels, namely one MR contrast and one PET channel. In addition, it showed only incremental improvements over conventional Frobenius norm-based vectorial TGV [3] (0.03 improved RMSE at best as reported in [20], with visual improvements still less perceptible). This would raise the question if the nuclear norm-based TGV is worth the extra computational workload (n^2 SVDs for a size- $n \times n$ image in each iteration) over Frobenius norm TGV, already presented in [3].

The approach of [3] considered MC-PI-CS MRI via vectorial versions of TV and TGV. However, this paper presented only a few experiments, and even then, the superiority of MC-PI: TGV over MC-PI: TV was not as very prominent. In fact, the experiments of the proposed paper (presented in Section III) suggest that MC-PI: TGV does not offer a statistically meaningful improvement over MC-PI: TV. A method that stands out is still needed.

This paper's contribution: None of the methods listed above considered isotropy in a MC setting, and in fact, to the best of the author's knowledge, the potential benefits of isotropy has been totally ignored within MC frameworks. In a previous work [9], the *rotation invariant total variation* (RITV) was used to reconstruct single-contrast single-coil MR images $u \in \mathbb{R}^{n \times n}$ with

$$\begin{aligned} \text{RITV}(u) &= \min_{\{v_s: s \in S\}} \sum_{s \in S} \|v_s\|_{1,2} \\ \text{s.t. } &\sum_{s \in S} L_s^* v_s - Du = 0, \end{aligned} \quad (1)$$

where the set $S = \{\leftrightarrow, \updownarrow, \bullet, +\}$ symbolized image gradient field (GF) mesh grids, D was the conventional finite differences' operator and L_s were linear operators that interpolated GF images v_s on the new grids [14] such that the rotation-invariance (or isotropy) was satisfied [9]. In this paper, the main focus is on a novel extension of (1) to multi-channel images such that an arbitrary number of channels N are allowed (not just $N = 2$ as with many other works), the isotropy is still maintained, channel-specific details are preserved without leakage to other channels and performance is

This study did not receive any financial support.

The author is an independent researcher, 1417866191 Tehran, Iran (email: erfanebrahim@outlook.com).

improved meaningfully over other MC-PI-CS approaches in MRI. A convex optimization problem will model the proposed method, for which a new extension of the Mlitsky-Pock algorithm [13] is developed to obtain the unique solution.

The rest of the paper will be presented as follows : Section II puts forward the proposed method. Section III reports the experiments and Section IV makes the concluding remarks. In order to avoid usual ambiguities in the MRI literature, we agree to use the phrases ‘‘contrast’’ and ‘‘channel’’ synonymously. Likewise, the terms ‘‘parallel imaging’’ and ‘‘multi-coil imaging’’ are interchangeable. In particular, ‘‘multi-channel imaging’’ **never** refers to ‘‘parallel imaging’’.

II. PROPOSED FRAMEWORK

A. Theory

A trivial extension of (1) to a stack of multi-channel images $(u_c)_{c=1}^N$ would be channel-by-channel application of the regularization term; that is, $\text{RITV}((u_c)_1^N) = \sum_{c=1}^N \text{RITV}(u_c)$. However, such a naive formulation would not benefit from abundant redundancies and correlations among multiple contrast, such as potentially common edge locations or similar signal intensity transitions. Another useful prior information on all channels is that each contrast should have a fixed energy regardless of its rotational orientation. A regularization that takes these into factor is more likely to succeed.

Since most edge locations coincide on multi-channel images, it would be sensible to enforce sparsity on joint multi-channel pixel-wise gradient field directions. Indeed, it is known that reducing the number of linearly independent gradient directions at each pixel location (i, j) (or equivalently, increasing their linear dependence) would lead to aligned edges in pixel domain (see the simple but insightful example in Fig. 2 in [7]). We propose to do this by minimizing the nuclear norm of the pixel-wise joint N-channel GF matrix, since, minimization of nuclear norm promotes rank sparsity in this matrix, and hence, more linear dependence for pixel-wise gradient directions. For example, if pixel (i, j) is located in the interior of a constant (or highly smooth) region of all channels, then there is no common edge at (i, j) and the pixel-wise joint N-channel GF matrix will be entirely zero, and the singular values are trivially 0, the sparsest solution. On the other hand, if (i, j) is on a common edge in all N channels, then all GF directions are exactly the same, or exactly opposite, leading to a rank of 1, which is again the sparsest solution.

Based on the expectations above, the following extension of (1) is proposed ($c \in \mathcal{C} := \{1, \dots, N\}$ and $\|\cdot\|_*$ is the nuclear norm):

$$\begin{aligned} \text{NRITV}((u_c)_1^N) &= \min_{\{v_s^c\}} \sum_{s \in S} \sum_{i,j} \|(v_s^1(i,j) \cdots v_s^N(i,j))\|_* \\ \text{s.t.} \quad &\sum_{s \in S} L_s^* v_s^1 - Du_1 = 0, \\ &\vdots \\ &\sum_{s \in S} L_s^* v_s^N - Du_N = 0. \end{aligned} \quad (2)$$

The isotropy of (2) is asserted at once:

Proposition 1: Let \mathcal{R} be the operator that rotates each image channel by 90° . Then $\text{NRITV}(\mathcal{R}((u_c)_1^N)) = \text{NRITV}((u_c)_1^N)$.

The proof of Proposition 1 is outlined in the Appendix. Simply put, (2) proposes to enforce isotropy in each individual image channel by manipulating GF images in the constraints, and then sparsify the set of independent pixel-wise joint GF directions in the cost function, which would eventually lead to aligned edges. In MC-MRI, multiple channels usually show complementary information, where a feature or lesion might be observable in one contrast but invisible in another. Formulation (2) also takes this into consideration, because only sparse joint gradient directions are primarily promoted not gradient magnitudes, which, as we shall see in Section III, prevents leakage of a channel’s exclusive details into other channels. Note that for $N = 1$, NRITV reduces to RITV.

We are now ready for the multi-contrast multi-coil MRI compressed sensing model:

$$\begin{aligned} \min_{\{u_c \geq 0, v_s^c\}} \quad &\frac{1}{2} \sum_{c=1}^N \sum_{p=1}^P \|\mathcal{F}_p u_c - b_{c,p}\|_2^2 + \lambda \sum_{s \in S} \|(v_s^c)_{c=1}^N\|_{1,*} \\ \text{s.t.} \quad &\sum_{s \in S} L_s^* v_s^c - Du_c = 0; \quad c \in \{1, \dots, N\}, \end{aligned} \quad (3)$$

where P is the number of parallel coils, \mathcal{F}_p is the system matrix involving a partial Fourier operator and sensitivity modulation for coil p and λ is a balancing parameter. The restriction $u_c \geq 0$ prevents negative pixel values, modeling our interest in magnitude images.

Problem (3) is a convex minimization, which can be reformulated into a convex-concave saddle point problem as follows:

$$\begin{aligned} \min_{u_c, v_s^c} \max_{r_{c,p}} \quad &\lambda \sum_{s \in S} \|(v_s^c)_{c=1}^N\|_{1,*} + \sum_c \sum_p \langle \mathcal{F}_p u_c - b_{c,p}, r_{c,p} \rangle \\ &\sum_c \delta_{\{\mathbb{R}_+^n\}}(u_c) - \frac{1}{2} \sum_c \sum_p \|r_{c,p}\|_2^2 + \sum_c \delta_{\{0\}} \left(\sum_{s \in S} L_s^* v_s^c - Du_c \right) \\ &\iff \\ \min_{u_c, v_s^c} \max_{h_c, r_{c,p}} \quad &\lambda \sum_{s \in S} \|(v_s^c)_{c=1}^N\|_{1,*} + \sum_c \sum_p \langle \mathcal{F}_p u_c - b_{c,p}, r_{c,p} \rangle \\ &\sum_c \delta_{\{\mathbb{R}_+^n\}}(u_c) - \frac{1}{2} \sum_c \sum_p \|r_{c,p}\|_2^2 + \sum_c \langle \sum_{s \in S} L_s^* v_s^c - Du_c, h_c \rangle, \end{aligned} \quad (4)$$

where $\delta_A(u)$ is the indicator function of convex set A . By introducing the primal and dual variables x and y and the corresponding objective functions $g(x)$ and $f^*(y)$ respectively as $x^\top := (u_c, v_{\uparrow}^c, v_{\leftrightarrow}^c, v_{\bullet}^c, v_{\downarrow}^c)_{c=1}^N$, $y^\top := ((r_{c,p}, h_c)_{c=1}^N)_{p=1}^P$,

$$g(x) := \sum_c \delta_{\{\mathbb{R}_+^n\}}(u_c) + \lambda \sum_{s \in S} \|(v_s^c)_{c=1}^N\|_{1,*}, \quad (5)$$

$$f^*(y) := \frac{1}{2} \sum_c \sum_p \|r_{c,p}\|_2^2 + \sum_c \sum_p \langle b_{c,p}, r_{c,p} \rangle, \quad (6)$$

and

$$K := \begin{pmatrix} \mathcal{F} & 0 \\ -D & \mathcal{L}^* \end{pmatrix}, \quad (7)$$

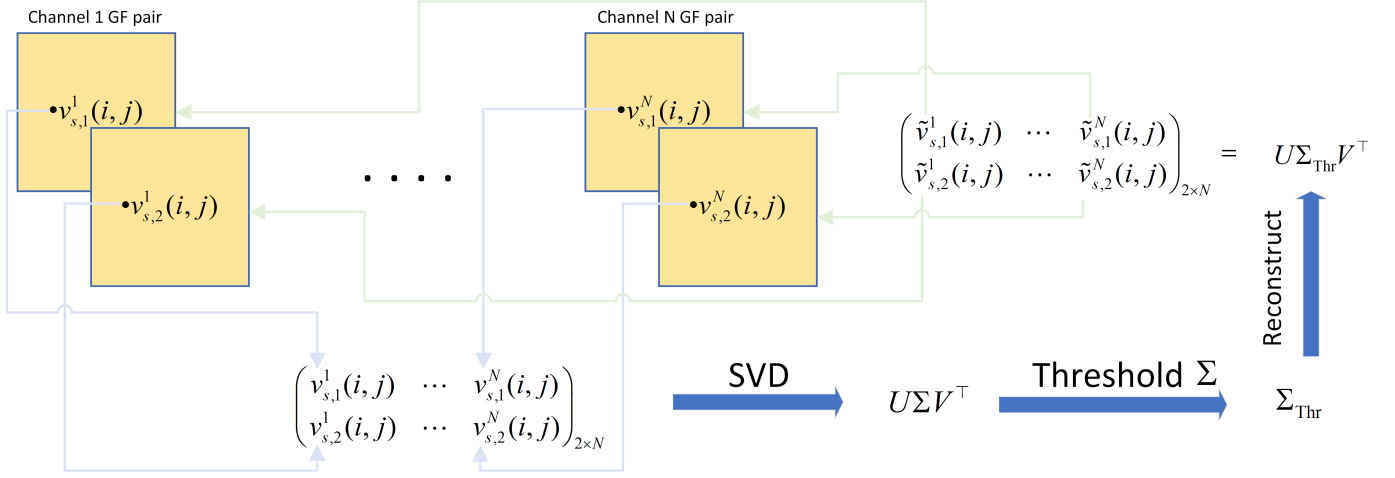


Fig. 1. Schematic representation of the solution for $\{v_s^c\}_{c=1}^N$ subproblem. For fixed i, j and s , GF values $v_s^c(i, j) = (v_{s,1}^c(i, j), v_{s,2}^c(i, j))$ are extracted from all channels c and arranged in order in the joint pixel-wise GF matrix. The SVD of this matrix is then taken, followed by soft-thresholding of the singular values. The matrix is subsequently reconstructed and each new GF value returns to its original position. The cycle has to repeat until i, j and s are exhausted.

where \mathcal{F} is an N -block-diagonal matrix with all coils' system matrices concatenated on each diagonal entry, \mathcal{D} is an N -block-diagonal matrix with D on each diagonal entry and \mathcal{L}^* is also an N -block-diagonal matrix with $[L_+^* L_-^* L_{\leftrightarrow}^* L_{\bullet}^* L_+^*]$ on each diagonal entry, we can develop the Malitsky-Pock algorithm [13] for (4).

B. Algorithm

1) *The u_c subproblem:* Update for each u_c is called a projection and given by

$$u_c^{k+1} = \max \{u_c^k - \tau_k (\sum_p \mathcal{F}_p^*(r_{c,p}^k) - D^*(h_c^k)), 0\}. \quad (8)$$

2) *The v_s^c subproblem:* This part is the core of the proposed algorithm and the crossroads where all N channels exchange information and joint GF update takes place. It is well known that for a separable function, the proximal operator decouples into a concatenation of the proximities of its components [10]. Invoking this result multiple times and setting $(\nu_s^{c,k})_{c=1}^N := (v_s^{c,k})_{c=1}^N - \tau_k (L_s(h_c^k))_{c=1}^N$, we obtain for each $s \in S$:

$$\begin{aligned} (v_s^{c,k+1})_{c=1}^N &= \text{prox}_{\tau_k \lambda \|\cdot\|_*}((\nu_s^{c,k})_{c=1}^N) \\ &= \left(\text{prox}_{\tau_k \lambda \|\cdot\|_*}(\nu_s^{c,k}(i, j))_{c=1}^N \right)_{i,j=1}^n \\ &= \left(\text{prox}_{\tau_k \lambda \|\cdot\|_*} \begin{pmatrix} \nu_{s,1}^{1,k}(i, j) & \cdots & \nu_{s,1}^{N,k}(i, j) \\ \nu_{s,2}^{1,k}(i, j) & \cdots & \nu_{s,2}^{N,k}(i, j) \end{pmatrix} \right)_{i,j=1}^n. \end{aligned} \quad (9)$$

Therefore, for fixed i, j and s , SVD of the joint pixel-wise GF matrix should be computed, followed by soft-thresholding of the singular values by $\tau_k \lambda$ and reconstructing the new GF matrix. The procedure is schematically represented in Fig. 1.

3) *The y subproblem:* This subproblem encompasses $r_{c,p}$ and h_c updates, given respectively by

$$r_{c,p}^{k+1} = \text{prox}_{\beta \tau_{k+1} (\frac{1}{2} \|\cdot\|_2^2 + \langle \cdot, b_{c,p} \rangle)}(r_{c,p}^k + \beta \tau_{k+1} \mathcal{F}_p(\bar{u}_c^{k+1})), \quad (10)$$

$$h_c^{k+1} = h_c^k + \beta \tau_{k+1} (-D(\bar{u}_c^{k+1}) + \sum_{s \in S} L_s^*(\bar{v}_s^{c,k+1})). \quad (11)$$

Algorithm 1 Proposed method for compressed multi-contrast parallel MRI

Initialization: Choose $\theta_0 = 1$, $u_c^0 = u_c^{\text{zf}}$, $v_s^{c,0} = 0$, $h_c^0 = 0$, $r_c^0 = 0$ for $s \in S$ and $c \in \mathcal{C} := \{1, \dots, N\}$, $\tau_0 > 0$, $\beta > 0$, $\mu \in (0, 1)$ and $\delta \in (0, 1)$. Define $\mathcal{P} := \{1, \dots, P\}$.

While convergence criterion not met, repeat:

- 1: Obtain u_c^{k+1} from (8) for each $c \in \mathcal{C}$;
- 2: Obtain $\{v_s^{c,k+1}\}_{c=1}^N$ jointly from (9) for each $s \in S$;
- 3: Choose $\tau_{k+1} \in [\tau_k, \tau_k \sqrt{1 + \theta_k}]$;
- Linesearch:**
- 4: $\theta_{k+1} = \frac{\tau_{k+1}}{\tau_k}$;
- 5: $\bar{u}_c^{k+1} = u_c^{k+1} + \theta_{k+1}(u_c^{k+1} - u_c^k)$, $\forall c \in \mathcal{C}$;
- 6: $\bar{v}_s^{c,k+1} = v_s^{c,k+1} + \theta_{k+1}(v_s^{c,k+1} - v_s^{c,k})$, $\forall s \in S, c \in \mathcal{C}$;
- 7: Obtain $r_{c,p}^{k+1}$ from (10) for each $c \in \mathcal{C}$ and $p \in \mathcal{P}$;
- 8: Obtain h_c^{k+1} from (11) for each $c \in \mathcal{C}$;
- 9: **if** $\sqrt{\beta} \tau_{k+1} \|(\{\mathcal{F}_p^*(r_{c,p}^{k+1} - r_{c,p}^k)\}_{c,p}, \{L_s(h_c^{k+1} - h_c^k)\}_{s,c})\|_2 \leq \delta \|(\{r_{c,p}^{k+1} - r_{c,p}^k, h_c^{k+1} - h_c^k\}_{c,p})\|_2$ **then**
- 10: Return to step 1 (break linesearch),
- 11: **else**
- 12: Set $\tau_{k+1} = \mu \tau_{k+1}$ and return to step 4 (apply another iteration of linesearch).
- 13: **end if**

Output: Reconstructed stack of multi-contrast MR images $\{u_c\}_{c=1}^N$, solution to (3).

The proposed method is summarized in Algorithm 1. The convergence of the algorithm to the unique solution of (4) is already elegantly proven in [13].

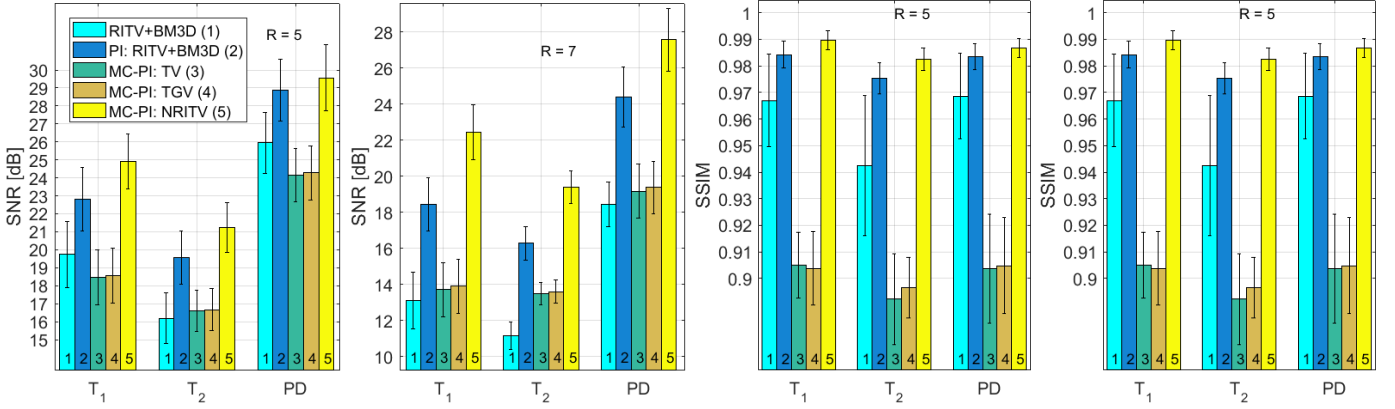


Fig. 2. Statistical summary of BrainWeb Experiments.

III. EXPERIMENTS

A. Setup

In this section the proposed framework will be validated. All tests run on data obtained BrainWeb [23] and Cancer Imaging Archive [24]. All simulations were conducted in MATLAB R2016a on a PC with an AMD FX-7600 Radeon R7 CPU at 2.70 GHz clock speed, AMD R9 M280X GPU with 4GB of memory and 8GB of RAM. Five methods are considered for comparison:

- 1) The single-contrast single-coil method of [9], **RITV + BM3D**. The parameters of [9] carry over.
- 2) A modified version of [9] where PI is considered, **PI: RITV + BM3D**. The parameters of [9] carry over, but the partial Fourier transform is replaced by multi-coil system matrices, and the corresponding dual variable r is modified accordingly. This method is one of the minor contributions of this paper.
- 3) The **MC-PI: TV** method of [3]. The parameters carry over, however the stopping criterion was modified so that either a maximum number of 500 iterations was reached or a relative error of less than 10^{-5} between two successive iterations or a change of less than 10^{-5} in the objective function was observed. This change was made to ensure more iterations than originally intended by the authors of [3], so that a better solution is obtained.
- 4) The **MC-PI: TGV** method of [3]. In the experiments of the presented paper, this method did not produce acceptable results at its default parameter settings (it was outperformed by MC-PI: TV). In order to improve this, μ was optimized to 10^{-2} . The stopping criterion was modified as in MC-PI: TV.
- 5) The proposed framework in the present paper, tagged **MC-PI: NRITV**. The parameters are set as $\beta = 4 \times 10^{-5}$, $\lambda = 7 \times 10^{-5}$, $\mu = 0.7$, $\delta = 0.99$ and $\theta_0 = 1$.

Methods 1, 2 and 5 run for 300 iterations and all methods are initialized with the zero-filling solution. We were eager to provide comparisons with the recent method of [6] as well but a software was not available from the first author of that work.

A virtual array of 8 coils was simulated by generating sensitivity maps using the eigenvalue approach of ESPIRiT [22]. Cartesian sampling patterns with fairly aggressive reduction

factors of $R = 5, 7$ and 9 are used in the experiments. This is for two reasons: first, Cartesian patterns are by far the most popular patterns in real-life clinical applications and a purpose of the present work was to stick as closely as possible to clinical protocols, and secondly, with highly incoherent patterns like variable density random or spiral, all MC-PI methods produce almost ground-truth-quality results (even at very aggressive reduction factors), in which case not much of a competition would be left among different methods.

MATLAB codes reproducing the proposed method will be released at [25] in the event that the manuscript is accepted or returned for minor revision. The quality of reconstructions is quantified by SSIM (MATLAB's built-in function) and $\text{SNR}(u, u_{\text{true}}) = 10 \log \frac{\|u\|_2}{\|u - u_{\text{true}}\|_2}$.

B. Results

1) *BrainWeb data*: In order to obtain a firm idea of the performance of the proposed framework, 60 multi-contrast slices distributed into triplets of T_1 -weighted, T_2 -weighted and proton-density scans of the normal brain were obtained from [23]. The mean (thick color bars) \pm standard deviation (narrow black bars) for all considered methods are reported in Fig. 2. The observations can be summarized as follows:

- 1) Comparison of RITV + BM3D with PI: RITV + BM3D reveals the benefits of PI in compressed MRI. This fact is well established in MRI community.
- 2) Comparison of PI: RITV + BM3D (method 2) with MC-PI: NRITV (method 5) reveals the interesting fact that although the proposed MC-PI: NRITV (method 5) does not benefit from the additional regularization provided by the BM3D frame, which is known to be a very elegant regularizer for MRI applications ([12], [21], [9]), it still outperforms method 2. This implies the power of the proposed MC regularization term, NRITV. In the MATLAB package associated to this paper, a variant of method 5 is also implemented which is equipped with a BM3D regularizer of the form $\sum_c \|\Phi(u_c)\|_0$. The author observed empirically that the addition of this regularization improves the error metrics of method 5 only marginally, which is not worthy of consideration.

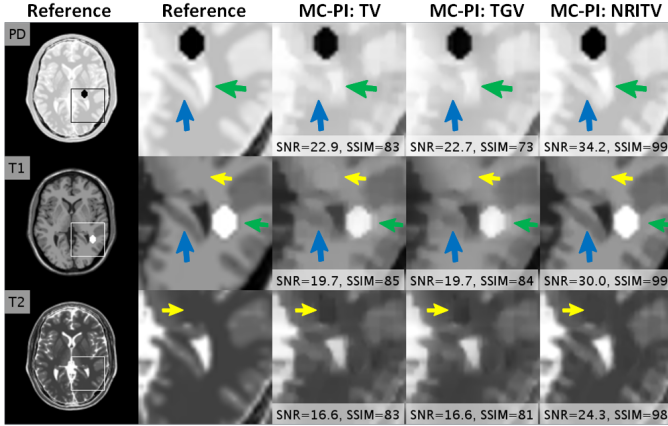


Fig. 3. Reconstructions for an example triplet from the BrainWeb dataset.

- 3) Comparison of MC-PI: TV (method 3) and MC-PI: TGTV (method 4) reveals little statistical superiority to TGTV.
- 4) Finally, comparison of methods 3 and 4 against method 5 attests to prominent superiority of the proposed method over TV and TGTV.

Fig. 3 illustrates an example from the BrainWeb test set. The size was changed to 200×200 for visualization and a sampling pattern with reduction factor of $R = 7$ was used. In order to simulate the situation where a lesion is observable in one contrast but invisible in others, a black hexagon in the PD contrast and a white hexagon in the T_2 contrast where superimposed to the images. Reconstruction results show several blatant errors with TV and TGTV solutions, some of which are annotated with arrows.

The yellow arrows in T_1 and T_2 results in Fig. 3 point to the location of the PD-only lesion. Severe leakage of this lesion to T_1 and T_2 contrasts are observable with TV and TGTV results whereas NRITV has almost entirely prevented such a leakage.

The green arrows in the T_1 results in Fig. 3 point to the right-side edges of the T_1 -only lesion. TV and TGTV have significantly blurred the edges on the right side of the lesion while with NRITV the edges are equally sharp on all sides. This shows the significance of isotropy in regularization, because the lesion is symmetric and hence invariant under 180° rotation. This observation is in line with those made by Condat [14], where it was discussed that TV does not sufficiently penalize oblique edges, leading to non-isotropy. The same could be said of TGTV, because the image gradient field used in TGTV is essentially the same as TV. This is also highlighted in Fig. 4 with line profiles. Due to symmetry in the lesion, intensity transitions when the line enters the lesion (about index 127, marked by the left rectangle) is almost the same as when the line leaves the lesion (about index 137, marked by the right rectangle). TV and TGTV fail to capture the intensity jump in the right side due to a lack of isotropy, while NRITV is almost indistinguishable from the symmetric reference profile.

Fig. 5 shows retrospective reconstructions of a 4-contrast in-vivo breast scan obtained from Cancer Imaging Archive [24]. The slices were resized to 200×200 and undersampled at $R = 9$. The proposed method again outperforms the other methods

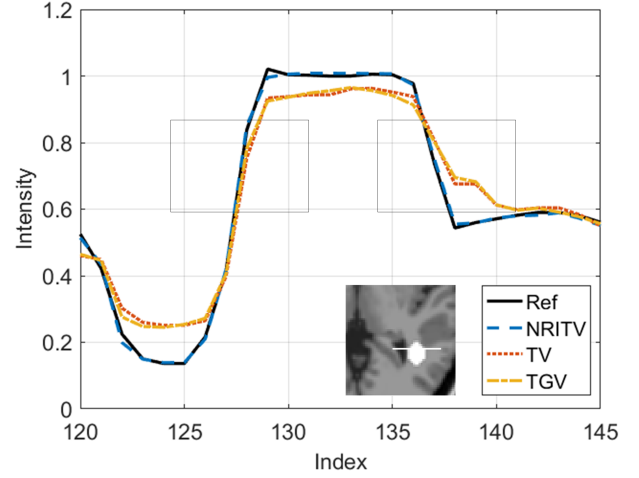


Fig. 4. Line profiles through the T_1 -only lesion. The left rectangle shows the sharp transition in intensity on the left side of the lesion (perfectly captured by NRITV, fairly by TV and TGTV), and the right rectangle shows the mirror transition on the right side of the lesion, perfectly captured by NRITV but poorly by TV and TGTV.

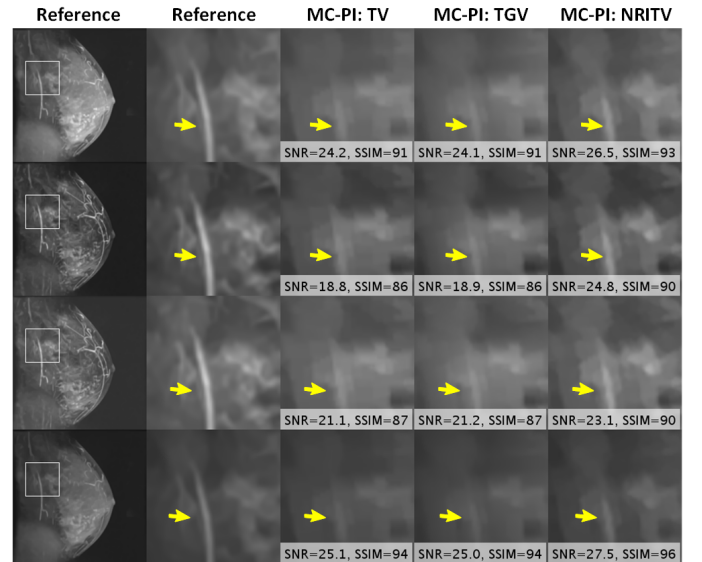


Fig. 5. Reconstructions for an example 4-contrast breast scan from Cancer imaging Archive.

with the best SNR and SSIM. The yellow arrows in this figure point to an example vessel which is poorly reconstructed in the other methods but easily recognizable with the proposed one.

IV. DISCUSSION AND CONCLUSIONS

In this article a novel isotropic multi-channel image regularizer was introduced within the context of compressed multi-contrast parallel MRI and a primal-dual algorithm with line-search was proposed to solve the new model. It was observed that this method significantly improves upon multi-channel TV and TGTV by virtue of inherent isotropy and leakage-prevention of channel-specific details.

The proposed method can easily carry over to other multi-channel image processing tasks such as color image deblurring or super resolution, as well as other multi-modality medical imaging applications such as PET-CT, MR-PET etc. In fact, the author's original intention was to propose this method within the context of multi-contrast MR-PET, however, test data sets for such modalities are rarely accessible to independent researchers, moreover, unlike the Fourier transform, a fast implementation of the PET system matrix does not appear to be publicly available (the private, non-open-source implementation of this operator is reported to take over 7 hours to run in [20]). Nevertheless, mathematically, the overall framework is hardly any different than proposed in the present paper; the only change would be the addition of Kullback-Leibler divergence to the cost function and assignment of the $N + 1$ 'st channel to the PET image.

Currently the non-optimized proof-of-principles implementation of the proposed method takes about 6 seconds to run on 4 contrasts at size 200×200 . This can significantly improve by an optimized, parallelized C++ transfer of the codes, particularly the SVDs which make up most of the computational task.

It was pointed out in Section III that the inclusion of channel-by-channel BM3D to the proposed method does not contribute meaningfully to the performance. However, the influence of a possible multi-channel BM3D transform where cross-channel correlations are exploited, remains to be investigated. A semblance of such a transform is already pointed out in [11] for color image processing, but it is restricted to the 3 color channels.

ACKNOWLEDGMENT

The author would like to thank all the researchers who share their reproducible work, in particular Dr. Itthi Chatnuntawech who made their software available upon the author's request.

APPENDIX

PROOF SKETCH FOR PROPOSITION 1

For any two dimensional digital image $u \in \mathbb{C}^{n \times n}$, $\mathcal{R}u(j, i) = u(i, n - j + 1)$. With this in mind, assume that $((v_s^c)_{c \in \mathcal{C}})_{s \in \mathcal{S}}$ is the solution to problem (2), which is known to exist uniquely by convexity. Consider the problem

$$\begin{aligned} \min_{\{\bar{v}_s^c: s \in \mathcal{S}, c \in \mathcal{C}\}} \lambda \sum_{s \in \mathcal{S}} \|(\bar{v}_s^c)_{c=1}^N\|_{1, \star} \\ \text{s.t. } \sum_{s \in \mathcal{S}} L_s^* \bar{v}_s^c - D(\mathcal{R}u_c) = 0; \forall c \in \mathcal{C}. \end{aligned} \quad (12)$$

It is easy to verify that the following solution satisfies the constraints in (12) for each $c \in \mathcal{C}$:

$$\begin{aligned} \bar{v}_\bullet^c &= (\bar{v}_{\bullet,1}^c, \bar{v}_{\bullet,2}^c) = (-\mathcal{R}v_{\bullet,2}^c, \mathcal{R}v_{\bullet,1}^c), \\ \bar{v}_\dagger^c(i, j) &= (\bar{v}_{\dagger,1}^c(i, j), \bar{v}_{\dagger,2}^c(i, j)) \\ &= (-\mathcal{R}v_{\leftrightarrow,2}^c(i+1, j), \mathcal{R}v_{\leftrightarrow,1}^c(i+1, j)), \\ \bar{v}_{\leftrightarrow}^c &= (\bar{v}_{\leftrightarrow,1}^c, \bar{v}_{\leftrightarrow,2}^c) = (-\mathcal{R}v_{\downarrow,2}^c, \mathcal{R}v_{\downarrow,1}^c) \\ \bar{v}_\uparrow^c &= (\bar{v}_{\uparrow,1}^c, \bar{v}_{\uparrow,2}^c) = (-\mathcal{R}v_{\uparrow,2}^c, \mathcal{R}v_{\uparrow,1}^c). \end{aligned}$$

It remains to show that

$$\sum_{s \in \mathcal{S}} \| (v_s^c)_{c=1}^N \|_{1, \star} = \sum_{s \in \mathcal{S}} \| (\bar{v}_s^c)_{c=1}^N \|_{1, \star}. \quad (13)$$

For $s = \bullet$, we have

$$\begin{aligned} \| (\bar{v}_\bullet^c)_{c=1}^N \|_{1, \star} &= \sum_{i,j=1}^n \left\| \begin{pmatrix} -\mathcal{R}v_{\bullet,2}^1 & \cdots & -\mathcal{R}v_{\bullet,2}^N \\ \mathcal{R}v_{\bullet,1}^1 & \cdots & \mathcal{R}v_{\bullet,1}^N \end{pmatrix} \right\|_{\star} \\ &= \sum_{i,j} \left\| \begin{pmatrix} -v_{\bullet,2}^1(i, n-j+1) & \cdots & -v_{\bullet,2}^N(i, n-j+1) \\ v_{\bullet,1}^1(i, n-j+1) & \cdots & v_{\bullet,1}^N(i, n-j+1) \end{pmatrix} \right\|_{\star} \\ &= \sum_{i,j} \left\| \begin{pmatrix} -v_{\bullet,2}^1(i, j) & \cdots & -v_{\bullet,2}^N(i, j) \\ v_{\bullet,1}^1(i, j) & \cdots & v_{\bullet,1}^N(i, j) \end{pmatrix} \right\|_{\star} = \| (v_\bullet^c)_{c=1}^N \|_{1, \star}. \end{aligned}$$

Similarly, one has $\| (\bar{v}_\dagger^c)_{c=1}^N \|_{1, \star} = \| (v_\dagger^c)_{c=1}^N \|_{1, \star}$, $\| (\bar{v}_{\leftrightarrow}^c)_{c=1}^N \|_{1, \star} = \| (v_{\leftrightarrow}^c)_{c=1}^N \|_{1, \star}$ and $\| (\bar{v}_{\uparrow}^c)_{c=1}^N \|_{1, \star} = \| (v_{\uparrow}^c)_{c=1}^N \|_{1, \star}$. Eq. (13) follows by summing these terms. \square

REFERENCES

- [1] M. Lustig, D. Donoho, J. Santos, and J. Pauly, *Compressed Sensing MRI*, IEEE Signal Processing Magazine, vol. 25, no. 2, pp. 72-82, 2008.
- [2] J. F. Glockner, H. H. Hu, D. W. Stanley, L. Angelos and K. King *Parallel MR imaging: a user's guide*, Radiographics, vol. 25, no. 5, pp. 1279-1297, 2005.
- [3] I. Chatnuntawech, A. Martin, B. Bilgic, K. Setsompop, E. Adalsteinsson and E. Schiavi, *Vectorial total generalized variation for accelerated multi-channel multi-contrast MRI*, Magnetic Resonance Imaging, vol. 34, pp. 1161-1170, 2016.
- [4] F. Knoll, K. Bredies, T. Pock and R. Stollberger, *Second order total generalized variation (TGV) for MRI*, Magnetic Resonance in Medicine, vol. 65, no. 2, pp. 480-491, 2011.
- [5] P. Blomgren and T. F. Chan, *Color TV: total variation methods for restoration of vector-valued images*, IEEE Transactions on Image Processing, vol. 7, no. 3, pp. 304-309, 1998.
- [6] E. Kopanoglu, A. Gungor, T. Kilic, E. U. Saritas, K. K. Oguz, T. Cukur et al, *Simultaneous use of individual and joint regularization terms in compressive sensing: Joint reconstruction of multi-channel multi-contrast MRI acquisitions*, NMR in Biomedicine, vol. 33, no. 4, e4247, 2020.
- [7] D. S. Rigie and P. J. La Riviere, *Joint reconstruction of multi-channel, spectral CT data via constrained total nuclear variation minimization*, Physics in Medicine & Biology, vol. 60, no. 5, pp. 1741-1762, 2015.
- [8] M. J. Ehrhardt and M. M. Betcke, *Multi-contrast MRI reconstruction with structure-guided total variation*, SIAM Journal on Imaging Sciences, vol. 9, no. 3, pp. 1084-1106, 2016.
- [9] E. E. Esfahani and A. Hosseini, *Compressed MRI reconstruction exploiting a rotation-invariant total variation discretization*, Magnetic Resonance Imaging, doi: 10.1016/j.mri.2020.03.008, 2020.
- [10] A. Beck, *First-Order Methods in Optimization*, SIAM, Philadelphia, 2017.
- [11] K. Dabov, A. Foi, V. Katkovnik and K. Egiazarian, *Image denoising by sparse 3D transform-domain collaborative filtering*, IEEE Transactions on Image Processing, vol.16, no.8, pp. 2080-2095, 2007.
- [12] E. M. Eksioğlu, *Decoupled algorithm for MRI reconstruction using nonlocal block matching model: BM3D-MRI*, Journal of Mathematical Imaging and Vision, vol. 56, no. 3, pp. 430-440, 2016.
- [13] Y. Malitsky and T. Pock, *A first-order primal-dual algorithm with linesearch*, SIAM Journal on Optimization, vol. 28, no. 1, pp. 411-432, 2018.
- [14] L. Condat, *Discrete total variation: new definition and minimization*, SIAM Journal on Imaging Sciences, vol. 10, no. 3, pp. 1258-1290, 2017.
- [15] Z. Zhan, J.-F. Cai, D. Guo, Y. Liu, Z. Chen and X. Qu, *Fast multiclass dictionary learning with geometrical directions in MRI reconstruction*, IEEE Transactions on Biomedical Engineering, vol. 63, no. 9, pp. 1850-1861, 2016.
- [16] Z. Lai, X. Qu, Y. Liu, D. Guo, J. Ye, Z. Zhan et al, *Image reconstruction of compressed sensing MRI using graph-based redundant wavelet transform*, Medical Image Analysis, vol. 27, pp. 93-104, 2016.
- [17] Y. Yang, J. Sun, H. Li, and Z. Xu, *Deep ADMM-Net for compressive sensing MRI*, in Proceedings of NIPS, pp. 10-18, 2016.

- [18] X. Qu, Y. Hou, F. Lam, D. Guo, J. Zhong and Z. Chen, *Magnetic resonance image reconstruction from undersampled measurements using a patch-based nonlocal operator*, *Medical Image Analysis*, vol. 18, no. 6, pp. 843-856, 2014.
- [19] X. Qu, D. Guo, B. Ning, Y. Hou, Y. Lin, S. Cai et al, *Undersampled MRI reconstruction with patch-based directional wavelets*, *Magnetic Resonance Imaging*, vol. 30, no. 7, pp. 964-977, 2012.
- [20] F. Knoll, M. Holler, T. Koesters, R. Otazo, K. Bredies and D. K. Sodickson, *Joint MR-PET reconstruction using a multi-channel image regularizer*, *IEEE Transactions on Medical Imaging*, vol. 36, no. 1, pp. 1-16, 2017.
- [21] E. M. Eksioğlu and A. K. Tanc, *Denoising AMP for MRI reconstruction: BM3D-AMP-MRI*, *SIAM Journal on Imaging Sciences*, vol. 11, no. 3, pp. 2090-2109, 2018.
- [22] M. Uecker, P. Lai, M. J. Murphy, P. Virtue, M. Elad, J. M. Pauly et al. *ESPIRiT—an eigenvalue approach to autocalibrating parallel MRI: where SENSE meets GRAPPA*, *Magnetic Resonance in Medicine*, vol. 71, no. 3, pp. 990-1001, 2014.
- [23] *BrainWeb*, <https://brainweb.bic.mni.mcgill.ca/brainweb/>, Online, accessed May 2020.
- [24] *Cancer Imaging Archive*, <https://www.cancerimagingarchive.net/>, Online, accessed May 2020.
- [25] E. E. Esfahani, *Data for: A multi-channel framework for joint reconstruction of multi-contrast parallel MRI*, Online, doi:10.17632/cwfb5m634x.1, 2020.